The Astronomical Journal, 162:285 (16pp), 2021 December https://doi.org/10.3847/1538-3881/ac2ccd

Orbital Parameters and Binary Properties of 37 FGK Stars in the Cores of Open Clusters NGC 2516 and NGC 2422

Isabel Lipartito[1], John I. Bailey III[1], Timothy D. Brandt[1], Benjamin A. Mazin[1], Mario Mateo[2], Meghin E. Spencer[2], and Ian U. Roederer[2,3]
[1] Department of Physics, University of California, Santa Barbara Santa Barbara, CA 93106, USA; baileyji@ucsb.edu
[2] Department of Astronomy, University of Michigan Ann Arbor, MI 40109, USA
[3] Joint Institute for Nuclear Astrophysics—Center for the Evolution of the Elements (JINA-CEE), USA
Received 2021 April 27; revised 2021 September 22; accepted 2021 September 23; published 2021 December 3

Abstract

We present orbits for 24 binaries in the field of open cluster NGC 2516 (∼150 Myr) and 13 binaries in the field of open cluster NGC 2422 (∼130 Myr) using results from a multiyear radial-velocity (RV) survey of the cluster cores. Six of these systems are double-lined spectroscopic binaries. We fit these RV variable systems with `orvara`, a MCMC-based fitting program that models Keplerian orbits. We use precise stellar parallaxes and proper motions from Gaia EDR3 to determine cluster membership. We impose a barycentric RV prior on all cluster members; this significantly improves our orbital constraints. Two of our systems have periods between five and 15 days, the critical window in which tides efficiently damp orbital eccentricity. These binaries should be included in future analyses of circularization across similarly-aged clusters. We also find a relatively flat distribution of binary mass ratios, consistent with previous work. With the inclusion of TESS light curves for all available targets, we identity target 378–036252 as a new eclipsing binary. We also identify a field star whose secondary has a mass in the brown dwarf range, as well as two cluster members whose RVs suggest the presence of an additional companion. Our orbital fits will help constrain the binary fraction and binary properties across stellar age and across stellar environment.

Unified Astronomy Thesaurus concepts: Radial velocity (1332); Computational methods (1965); Astronomical methods (1043); Astronomy data analysis (1858); Open star clusters (1160); Spectroscopy (1558); Binary stars (154); Orbits (1184)

Supporting material: machine-readable tables, figure set

1. Introduction

Stellar multiplicity is ubiquitous: nearly all high-mass stars live in binaries (Duchêne & Kraus 2013) and around half of nearby solar-mass field stars are binaries (Raghavan et al. 2010). It is also a function of environment: binaries in dense environments are especially subject to dynamical evolution with interactions changing or disrupting their orbits (Binney & Tremaine 2008). Indeed, binaries (and higher-order systems) are rarer in dense globular clusters, where frequent, strong dynamical encounters serve to disrupt wide binaries and harden tight binaries (Vesperini et al. 2011, 2013; Lucatello et al. 2015). Such encounters are rarer in the less dense environments of open clusters (Portegies Zwart et al. 2010). Yet spectroscopic and photometric surveys of open clusters show total observed binary fractions ranging from 13% to 70% for solar-type stars (Sollima et al. 2010; Duchêne & Kraus 2013), while NGC 2516 could have a total binary fraction as high as 85% (Jeffries et al. 2001). The binary fraction does not appear to show a clear dependence on the cluster's age, density, or chemical composition (Portegies Zwart et al. 2010; Duchêne & Kraus 2013).

Open clusters are conatal, coeval environments through which we can explore stellar multiplicity as a universal outcome of star formation (Goodwin 2010). The properties of stellar binaries in open clusters may be used to probe a cluster's initial conditions. For example, Griffiths et al. (2018) discussed how the presence of massive binaries on wide orbits gives insight to the cluster's initial density and structure.

Astrophysical parameters, luminosity functions, and stellar orbital properties have also been studied across clusters (e.g., Kharchenko et al. 2005, 2009, 2013; Griffin 2012). The period distribution for binaries with solar-type primary stars in open clusters appears to be broad and unimodal over the range of 1 day to 10^4 yr (Duchêne & Kraus 2013). Wider binaries are much rarer: only two to three percent of stars with masses between 0.5 $M_\odot$ and 1.5 $M_\odot$ have binary companions on orbits between 300 and 3000 au (Deacon & Kraus 2020). The mass ratio distribution for solar-type stars is approximately flat for both spectroscopic and visual binaries, and substellar companions appear to be rare (Duchêne & Kraus 2013).

Clusters are prime candidates for spectroscopic surveys due to the close grouping of the targets. Precision spectroscopic measurements enable characterization of the cluster chemical environment by determining elemental abundances (e.g., Bailey et al. 2018; Donor et al. 2020; Poovelil et al. 2020). Characterization of a clusters chemical environment further informs simulations of the clusters natal environment (e.g., Geller et al. 2013; Geller 2013; Geller et al. 2015). Precise stellar radial velocities (RVs) obtained through modeling spectral lines enable identification of binaries in open clusters (e.g., Sales Silva et al. 2014; Badenes et al. 2018; Martinez et al. 2020) and constraints on a cluster's multiplicity fraction (e.g., Guerrero et al. 2015; Kounkel et al. 2016; Nine et al. 2020). Notably, González & Lapasset 2000 used echelle spectroscopy to observe bright stars in NGC 2516, finding a binary fraction above 26% among high-mass main-sequence stars. Meanwhile, absolute astrometry from Gaia has enabled a

Table 1
Cluster Properties

System	NGC 2516	NGC 2422
Age (Myr)	120–150	74–130
Distance (pc)	415	487
$N_{\rm Mem}$	2518	907
$R_{\rm core}$ (pc)	$0.90^{+0.23}_{-0.17}$	1.58 ± 0.75
Cluster RV (km s^{-1})	24.50 ± 0.12	35.97 ± 0.09
$\sigma_{\rm RV}$ (m s^{-1})	734 ± 104	750 ± 65
Stellar Jitter (m s^{-1})	74 ± 9	138 ± 2
[Fe/H] (dex)	-0.08 ± 0.01	-0.05 ± 0.02
[α/Fe] (dex)	0.03 ± 0.01	0.02 ± 0.01
Binary Fraction (%)	100^{+0}_{-15}	62 ± 16

Note. Age as described in Section 2.3; 150 and 130 Myr are upper limits. Distance and membership are per Gaia Collaboration et al. (2018). Core radii derived from King profile modeling for 0.87–1.48 $M_\odot$ stars for NGC 2516 (Jeffries et al. 2001) and 0.7–1.0 $M_\odot$ stars for NGC 2422 (Prisinzano et al. 2003). Everything else per B18. $\sigma_{\rm RV}$ is the cluster-velocity dispersion.

far more detailed picture of Galactic open clusters, with distances and proper motions, photometry, and astrometric membership determinations (Gaia Collaboration et al. 2016; Cantat-Gaudin et al. 2018; Gaia Collaboration et al. 2018). Gaia's Early Third Data Release (EDR3; Gaia Collaboration et al. 2021; Lindegren et al. 2021) offers a factor of ∼2–4 improvement in astrometric precision over DR2, promising even better results. With snapshots of diverse systems at different ages in well-characterized environments, we can assemble a more complete picture of stellar multiplicity.

In this paper, we build upon previous work completed by Bailey et al. (2016; hereafter B16) and (2018; hereafter B18) exploring multiplicity in the open clusters NGC 2516 and NGC 2422. B16 obtained multiepoch spectroscopy for all stars with colors consistent with F5-K5 in a half-degree field centered on each of these clusters, identifying 40 and 22 RV binaries in the fields of NGC 2516 and NGC 2422, respectively (B18). Here, we extend this work with orbital fits for the majority of these binaries.

In Section 2 we review relevant details from B16 and B18, present a new epoch for a subset of the sample, and describe an extension of the B16 modeling process to double-lined systems. We report cluster ages and distances as measured by Gaia Data Release 2, review membership in light of parallaxes and proper motions provided by Gaia Early Data Release 3, and give the details of our orbital fitting process. Section 3 describes the results of the orbital fits and Section 4 discusses orbital parameter trends. We conclude with Section 5.

2. Observations and Data Analysis

In the following subsections, we discuss the observations, data reduction, and orbital fitting for the 62 binaries in the fields of NGC 2516 and NGC 2422. Table 1 summarizes the cluster properties determined in B16 and B18, with updates from Gaia DR2 and EDR3 where relevant.

2.1. Observations

B16 obtained multiepoch spectroscopy in 2013 and 2014 for all photometric F5V-K5V members (N∼125 each) in the core half degree of the open clusters NGC 2516 and NGC 2422. They obtained ∼12 epochs (∼2 hr exposures) in NGC 2516 and ∼10 epochs (∼2.5 hr exposures) in NGC 2422, providing a temporal baseline of ∼1.1 yr. B16 used Michigan/Magellan Fiber System (M2FS, Mateo et al. 2012), a multiplexed high-resolution optical fiber-fed spectrograph—deployed at the Magellan/Clay 6.5 m telescope at Las Campanas Observatory—in its cross-dispersed echelle mode for order 49 (7160–7290 Å) to obtain a total of ∼2700 spectra. B16 selected order 49 for its combination of stellar and telluric absorption lines to provide a simultaneous RV and wavelength reference. Observations had a median $R \sim 50,000$ and a mean per-pixel signal-to-noise ratio (S/N) of 55. This configuration has a limiting RV precision of 25 m s^{-1}, with a median per-epoch precision of 80 m s^{-1}.

Here we incorporate an additional epoch for 36 stars in NGC 2516 obtained from a 3 hr exposure taken in February 2016 with a median S/N of ∼107, extending 33 of our targets to a baseline of ∼3.25 yr. This epoch benefits from a newer M2FS filter tailored to the measured optical blaze, significantly improving throughput albeit with a slightly different wavelength coverage of 7180–7360 Å. We reduce these spectra following B16.

2.2. Data Reduction

B18 fit model stellar spectra to the data in order to simultaneously extract each target's $T_{\rm eff}$, [Fe/H], [α/Fe], $v_r \sin i$ (stellar rotational velocity), and line-of-sight RV. They used the relation of Torres et al. (2010) to compute stellar masses, which we adopt herein, albeit updated with new SB2 spectral fits.

To obtain RVs for double-lined systems, we employed the reduction package from B16 in binary mode where the model is constructed using a pair of stellar spectra. In this mode, the model gains a second set of stellar parameters and a flux fraction parameter that sets the normalized flux ratio between the component stellar spectra. We first performed an initial round of fits where we held one $T_{\rm eff}$ fixed to that in B18, the other with that as a starting guess. We used the [Fe/H] and [α/Fe] values from B18 for both components throughout. The veiling and $v_r \sin i$ parameters were fixed to unity and zero for both stars. This first round was carefully supervised to determine initial RV guesses within ∼20 km s^{-1} (∼10 pixels) for all components. The spectra were then refit for stellar parameters, allowing $T_{\rm eff}$ (and the coupled $\log(g)$), $v_r \sin i$, and flux fraction to float while still holding veiling fixed (these parameters are presented in Table 2). We ensured component spectra remained associated with the same spectral source by checking stellar parameters (e.g., whether stellar temperatures flipped) and by refitting each spectrum with the adopted stellar properties intentionally flipped to check for an improved chi square. We also separately validated this by fitting Keplerian orbits (Section 2.4) to the absolute value of the RV difference, $|{\rm RV}_1 - {\rm RV}_2|$. This approach obtained the correct orbital parameters even if several spectra were assigned to the wrong source; we could then check the source identification. We adopted stellar parameters and flux fraction as described in B16 but excluding fits with RVs closer than 1.5 resolution elements. We then performed a final round of fits to determine RVs with the adopted stellar parameters and flux fraction constant, but allowing veiling to float for each component.

We got successful two-component fits for targets 146-012622, 147-012265, 147-012499, 377-035049, 378-036176, and of which were identified as SB2s in B18–as well as

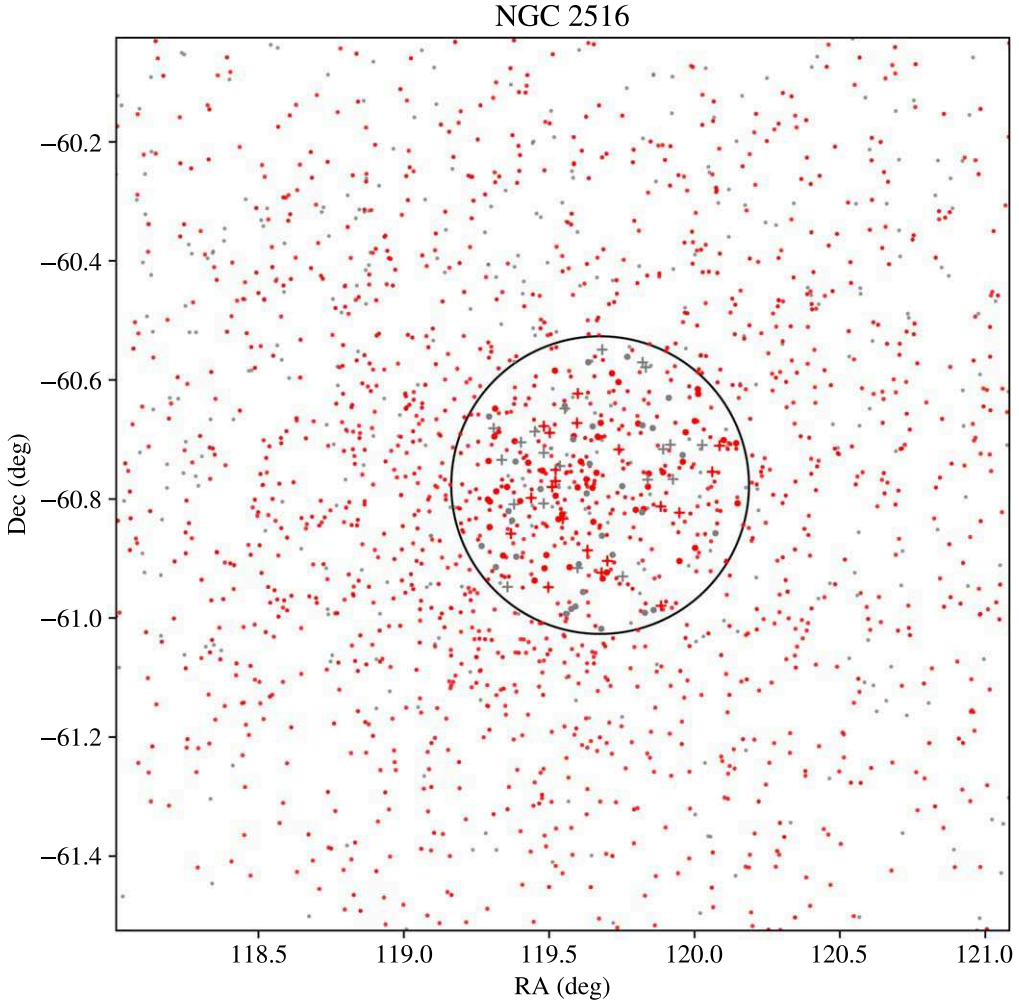

Figure 1. The NGC 2516 Field. The solid black circle marks the half-degree M2FS FOV. Red and gray points indicate membership and nonmembership, respectively, based on EDR3 astrometry (for M2FS targets studied in this paper) or DR2 (all else; Gaia Collaboration et al. 2018). Larger symbols indicate M2FS targets and crosses indicate those that are RV variable.

Table 2
Stellar Properties for SB2 Targets

Target ID	$T_{\rm eff}$ 1 (K)	$T_{\rm eff}$ 2 (K)	log(g) 1	log(g) 2	[Fe/H] (dex)	[α/Fe] (dex)	$v_r \sin i$ 1 (km s^{-1})	$v_r \sin i$ 2 (km s^{-1})	Flux 1 (%)
146–012622	5602 ± 22	5473 ± 21	4.54	4.55	−0.57	0.10	7.5 ± 0.2	6.5 ± 0.1	53 ± 1
147–012265	6273 ± 29	5538 ± 88	4.43	4.54	−0.25	0.04	16.4 ± 0.1	13.8 ± 0.6	80 ± 1
147–012499	5242 ± 16	4904 ± 29	4.58	4.62	−0.36	0.06	4.9 ± 0.2	10.1 ± 0.2	61 ± 0
377–035049	4881 ± 30	4756 ± 23	4.61	4.63	−0.24	0.06	2.7 ± 0.5	2.8 ± 0.6	54 ± 1
378–036176	6151 ± 46	5982 ± 19	4.46	4.48	−0.44	0.06	6.6 ± 0.1	5.6 ± 0.1	57 ± 1
378–036252	6281 ± 24	4879 ± 78	4.43	4.63	−0.14	0.02	9.1 ± 0.1	6.0 ± 0.5	89 ± 0

379-035982 and 147-012164–two SB2s that were missed in B18. We were not able to get reliable orbits for these last two SB2s, as they appear to be higher-order systems whose details we will discuss in Section 3. Stellar and fit properties of these stars are reported in Table 2.

Two stars reported as SB2 in B18, 147-012424 and 379-035886, proved impossible to fit for a second stellar component. Both were identified as nonmembers by Gaia (see next section). On further review of their spectra we now believe these to be off main sequence, possibly chemically peculiar stars with a significant number of unfit lines. We treated them as SB1s in our analysis, and ultimately excluded 379-035886 for poor data quality.

2.3. Cluster Properties and Gaia EDR3 Membership

B16 targeted NGC 2516, a 120–150 Myr cluster (Meynet et al. 1993; Sung et al. 2002; Kharchenko et al. 2005; Fritzewski et al. 2020) at 415 pc (Gaia Collaboration et al. 2018) and NGC 2422, a 74–130 Myr cluster (Loktin et al. 2001;

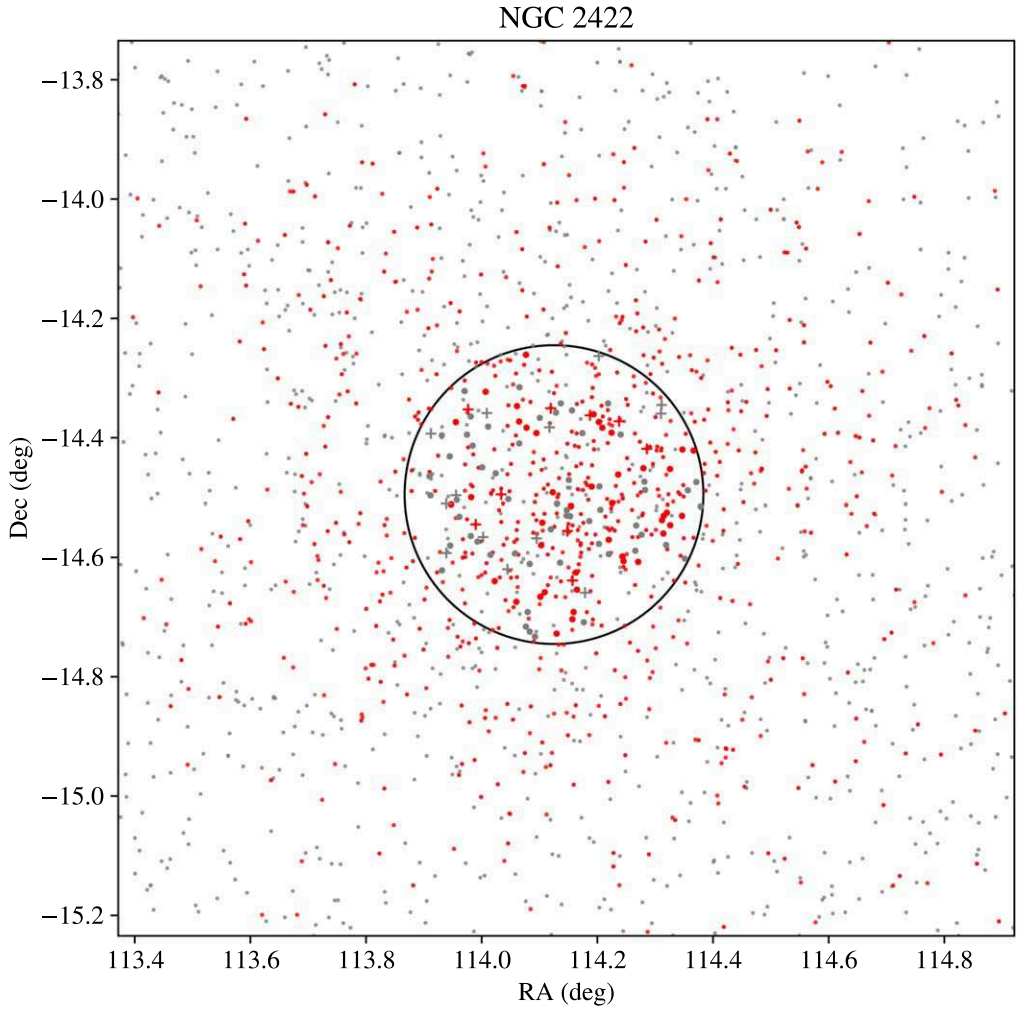

Figure 2. The NGC 2422 Field. The solid black circle marks the half-degree M2FS FOV. Red and gray points indicate membership and nonmembership, respectively, based on EDR3 astrometry (for M2FS targets studied in this paper) or DR2 (all else; Gaia Collaboration et al. 2018). Larger symbols indicate M2FS targets and crosses indicate those that are RV variable.

Kharchenko et al. 2005) at 487 pc (Gaia Collaboration et al. 2018) for a balance of astrophysical and instrumental reasons described therein. Gaia Collaboration et al. (2018) used Gaia DR2 photometry to derive cluster ages by fitting color–magnitude diagrams. While this gave an age consistent with prior works for NGC 2422 (130 Myr), it gave NGC 2516 an age of 300 Myr, far above the age range found previously. Moreover, it did not include several luminous, mid-B-type stars confirmed as members in the new Gaia analysis. Fritzewski et al. (2020) find that NGC 2516's rotation period distribution is comparable to that of the Pleiades, confirming an age of $\lesssim$150 Myr.

Figures 1 and 2 show all Gaia stars and M2FS targets in $1.^{\circ}5 \times 1.^{\circ}5$ fields centered on NGC 2516 and NGC 2422, respectively. We use red to indicate Gaia astrometric members as determined using EDR3 (for M2FS targets studied in this paper) or DR2 (all else; Gaia Collaboration et al. 2018), with larger symbols indicating M2FS targets and crosses indicating those that are RV variable. The solid black line marks the half-degree M2FS field of view (FOV).

While B18 used the mean stellar RV to determine membership, we are now able to rely exclusively on the precise astrometry of Gaia EDR3. A target was considered a cluster member if its parallax and proper motions from Gaia EDR3 (Gaia Collaboration et al. 2021) were within 5σ and 2 mas yr^{-1} respectively of the cluster parallaxes and proper motions from Gaia Collaboration et al. (2018). All of the astrometric member singles have mean stellar RVs within 5 km s^{-1} of the cluster RV, consistent with the scatter expected from measurement error, intrinsic velocity dispersion, and wide ($\gtrsim$5 au) binaries. In contrast, just 6 of 77 single stars that are astrometric nonmembers have RVs within 5 km s^{-1} of the cluster RV. The updates to membership in light of Gaia DR3 precision astrometry do not change the binary fraction within the margins of error reported by B18.

2.4. Orbital Fitting

We fit Keplerian orbits to our RVs using a custom adaptation of `orvara` (Brandt et al. 2021), a package for fitting stellar and exoplanet orbits using Markov chain Monte Carlo (MCMC) through the package `ptemcee` (Foreman-Mackey et al. 2013; Vousden et al. 2016). We ran our fits using 20 temperatures and 200 walkers with 1 million steps each; we fit for the orbital period P, eccentricity e, mean anomaly at a reference epoch $\lambda_{\rm ref}$, argument of periastron ω, RV semiamplitude K, and barycenter radial velocity RV_0. Our adaptation of `orvara` differs from the published version in its ability to analytically marginalize over K and ω, depending on the choice

Table 3
Binary Solutions in the Field of NGC 2516

Target ID	Mem.	$v \sin i$ (km s^{-1})	Period (days)	Ecc.	λ	ω	K (km s^{-1})	RV_0 (km s^{-1})	M ($M_\odot$)	q (M_2/M_1)	σ_χ
146-012358	N	4.48 ± 0.25	14.0683 ± 0.0010	$0.0083^{+0.0081}_{-0.0057}$	$1.8^{+3.4}_{-1.2}$	$1.3^{+1.2}_{-3.1}$	$11.670^{+0.10}_{-0.094}$	$69.464^{+0.086}_{-0.090}$	0.81	$0.182^{+0.11}_{-0.023}$	2.24
146-012365	M	6.339 ± 0.093	586^{+17}_{-21}	$0.865^{+0.026}_{-0.051}$	$3.35^{+0.24}_{-0.28}$	$-0.92^{+0.15}_{-0.20}$	$16.2^{+4.2}_{-4.1}$	$23.59^{+0.53}_{-0.57}$	1.04	$0.47^{+0.18}_{-0.11}$	1.21
146-012455	M	7.574 ± 0.060	$109.17^{+0.80}_{-2.0}$[a]	$0.252^{+0.072}_{-0.048}$	$2.16^{+0.32}_{-0.33}$	$-1.43^{+0.13}_{-0.20}$	$15.05^{+0.20}_{-0.17}$	$25.20^{+0.43}_{-1.0}$	0.89	$0.488^{+0.19}_{-0.052}$	1.72
146-012500	M	8.83 ± 0.23	$3.656213^{+0.000094}_{-0.000092}$	$0.0136^{+0.015}_{-0.0095}$	$3.3^{+1.9}_{-2.1}$	$0.2^{+2.0}_{-2.3}$	$24.15^{+0.66}_{-0.62}$	$24.31^{+0.32}_{-0.30}$	0.80	$0.249^{+0.14}_{-0.031}$	5.43
146-012557	N	4.93 ± 0.17	601^{+18}_{-46}[a]	$0.731^{+0.012}_{-0.034}$	$6.2668^{+0.0032}_{-0.0057}$	$-3.048^{+0.093}_{-0.032}$	$10.346^{+0.053}_{-0.050}$	$-26.87^{+0.10}_{-0.31}$	0.89	$0.401^{+0.19}_{-0.047}$	1.00
146-012601	M	16.07 ± 0.14	$1.868567^{+0.000043}_{-0.000039}$	$0.0051^{+0.0060}_{-0.0036}$	$4.05^{+0.89}_{-1.9}$	$0.01^{+1.8}_{-0.86}$	$30.37^{+0.22}_{-0.23}$	$25.096^{+0.057}_{-0.046}$	0.82	$0.247^{+0.14}_{-0.031}$	1.81
146-012622A	M	7.53 ± 0.16	$32.1170^{+0.0017}_{-0.0018}$	$0.1877^{+0.0021}_{-0.0020}$	$5.190^{+0.011}_{-0.010}$	-0.387 ± 0.012	$42.540^{+0.080}_{-0.079}$	24.0710 ± 0.0020	0.83	0.9659 ± 0.0019	1.19
146-012622B	⋯	6.52 ± 0.14	⋯	⋯	⋯	⋯	$44.040^{+0.081}_{-0.079}$	-0.81	⋯	⋯	
147-012175	M	10.83 ± 0.21	1033^{+492}_{-276}[a]	$0.42^{+0.34}_{-0.27}$	3.6 ± 1.4	$-1.61^{+4.4}_{-0.92}$	$5.2^{+6.1}_{-1.2}$	$24.32^{+0.69}_{-0.72}$	0.78	$0.35^{+0.24}_{-0.12}$	3.01
147-012205	N	3.967 ± 0.087	$\geqslant 128.70$[a]	⋯	⋯	⋯	⋯	$21.3^{+9.2}_{-5.3}$	1.01	$\geqslant 0.25$	6.34
147-012231	N	4.53 ± 0.44	$\geqslant 1243.58$[a]	⋯	⋯	⋯	⋯	$21.0^{+6.1}_{-2.3}$	0.92	$\geqslant 0.38$	4.96
147-012249	M	6.73 ± 0.10	23.2825 ± 0.0036	$0.1448^{+0.0085}_{-0.0084}$	$4.542^{+0.066}_{-0.064}$	$-2.431^{+0.069}_{-0.072}$	26.07 ± 0.22	23.898 ± 0.045	0.89	$0.522^{+0.19}_{-0.052}$	5.20
147-012262	M	4.61 ± 0.30	$27.647^{+0.014}_{-0.027}$	$0.62^{+0.23}_{-0.22}$	3.02 ± 0.16	-1.57 ± 0.15	$19.7^{+17}_{-6.1}$	24.49 ± 0.71	0.76	$0.36^{+0.17}_{-0.11}$	4.56
147-012265A	M	16.36 ± 0.14	$13.47942^{+0.00095}_{-0.00076}$	$0.6143^{+0.0028}_{-0.0027}$	$5.0877^{+0.0070}_{-0.0069}$	-2.1996 ± 0.0066	$61.18^{+0.27}_{-0.22}$	23.424 ± 0.040	1.12	0.7255 ± 0.0023	2.46
147-012265B	⋯	13.81 ± 0.63	⋯	⋯	⋯	⋯	$84.33^{+0.39}_{-0.31}$	⋯	0.81	⋯	⋯
147-012270	M	7.47 ± 0.56	333^{+247}_{-109}[a]	$0.43^{+0.16}_{-0.25}$	$4.9^{+1.1}_{-4.8}$	$0.6^{+2.0}_{-3.2}$	$11.4^{+3.5}_{-1.5}$	$24.50^{+0.72}_{-0.71}$	0.81	$0.57^{+0.21}_{-0.16}$	3.95
147-012290	N	3.36 ± 0.12	$\geqslant 617.62$[a]	⋯	⋯	⋯	⋯	$11.5^{+4.2}_{-1.1}$	0.88	$\geqslant 0.19$	2.14
147-012308	M	37.77 ± 0.23	$55.77^{+157}_{-0.12}$ [a]	$0.665^{+0.18}_{-0.037}$	$0.628^{+0.51}_{-0.093}$	$-1.850^{+0.72}_{-0.072}$	$11.93^{+13}_{-0.45}$	$25.08^{+0.76}_{-0.12}$	1.24	$0.226^{+0.31}_{-0.056}$	2.20
147-012424	N	6.39 ± 0.22	$23.1482^{+0.0047}_{-0.0046}$	$0.4649^{+0.0062}_{-0.0061}$	3.656 ± 0.012	-0.4886 ± 0.0088	$46.17^{+0.69}_{-0.66}$	17.79 ± 0.27	1.07	$0.831^{+0.092}_{-0.040}$	2.99
147-012432	M	5.875 ± 0.089	$\geqslant 576.26$	⋯	⋯	⋯	⋯	$24.36^{+0.74}_{-0.67}$	0.79	$\geqslant 0.50$	2.36
147-012433	N	4.06 ± 0.30	$\geqslant 256.90$[a]	⋯	⋯	⋯	⋯	$26.51^{+0.23}_{-1.6}$	0.85	$\geqslant 0.06$	1.00
147-012474	N	3.676 ± 0.087	$\geqslant 844.99$	⋯	⋯	⋯	⋯	$-1.6^{+5.2}_{-11}$	0.86	$\geqslant 0.41$	2.57
147-012487	M	10.38 ± 0.11	$16.3164^{+0.0026}_{-0.0027}$	0.034 ± 0.012	$5.70^{+0.34}_{-0.59}$	$1.52^{+0.41}_{-0.37}$	$18.27^{+0.38}_{-0.36}$	$23.77^{+0.24}_{-0.23}$	1.18	$0.275^{+0.16}_{-0.034}$	3.73
147-012499A	M	4.95 ± 0.21	$66.313^{+0.055}_{-0.050}$	0.416 ± 0.012	$1.798^{+0.039}_{-0.036}$	$0.305^{+0.020}_{-0.021}$	$30.77^{+0.56}_{-0.54}$	$24.956^{+0.080}_{-0.079}$	0.81	$0.943^{+0.014}_{-0.013}$	3.26
147-012499B	⋯	10.13 ± 0.16	⋯	⋯	⋯	⋯	$32.62^{+0.61}_{-0.60}$	⋯	0.77	⋯	⋯
148-012906	M	15.3 ± 1.0	747^{+10}_{-99}[a]	$0.22^{+0.26}_{-0.16}$	$4.96^{+0.70}_{-3.4}$	$0.1^{+1.0}_{-1.5}$	$8.9^{+2.5}_{-2.0}$	$24.47^{+0.70}_{-0.54}$	0.92	$0.55^{+0.22}_{-0.18}$	2.42
148-012940	N	5.955 ± 0.066	10.75742 ± 0.00019	$0.0021^{+0.0023}_{-0.0015}$	$3.9^{+1.5}_{-2.4}$	$0.2^{+1.4}_{-1.7}$	15.092 ± 0.047	$32.523^{+0.016}_{-0.015}$	1.13	$0.193^{+0.12}_{-0.025}$	1.00

Note.
[a] Denotes target with a multimodal fit.

(This table is available in its entirety in machine-readable form.)

Table 4
Binary Solutions in the Field of NGC 2422

Target ID	Mem.	$v \sin i$ (km s^{-1})	Period (days)	Ecc.	λ	ω	K (km s^{-1})	RV_0 (km s^{-1})	M ($M_\odot$)	q (M_2/M_1)	σ_χ
377-035049A	N	2.68 ± 0.54	18.9231 ± 0.0018	$0.0597^{+0.0073}_{-0.0070}$	$3.14^{+0.10}_{-0.11}$	$2.274^{+0.11}_{-0.093}$	46.06 ± 0.38	21.04 ± 0.13	0.77	0.993 ± 0.013	2.75
377-035049B	⋯	2.80 ± 0.64	⋯	⋯	⋯	⋯	46.40 ± 0.40	⋯	0.77	⋯	⋯
378-036136	N	9.02 ± 0.20	$\geqslant 591.51$	⋯	⋯	⋯	⋯	35.5 ± 1.4	0.92	$\geqslant 0.20$	1.00
378-036137	N	3.01 ± 0.22	$\geqslant 663.45$[a]	⋯	⋯	⋯	⋯	$119.96^{+1.3}_{-0.66}$	0.80	$\geqslant 0.07$	1.00
378-036176A	N	6.64 ± 0.12	8.63908 ± 0.00012	$0.00112^{+0.0011}_{-0.00078}$	$4.5^{+1.1}_{-3.0}$	$-1.4^{+3.4}_{-1.1}$	$46.398^{+0.061}_{-0.060}$	41.9173 ± 0.0026	1.03	0.9424 ± 0.0016	1.59
378-036176B	⋯	5.61 ± 0.14	⋯	⋯	⋯	⋯	49.234 ± 0.062	⋯	0.97	⋯	⋯
378-036252A	M	9.15 ± 0.13	7.28663 ± 0.00010	0.0079 ± 0.0014	$5.04^{+0.22}_{-0.21}$	$1.46^{+0.21}_{-0.22}$	54.39 ± 0.11	34.510 ± 0.018	1.15	0.6418 ± 0.0014	1.37
378-036252B	⋯	6.04 ± 0.51	⋯	⋯	⋯	⋯	84.73 ± 0.16	⋯	0.74	⋯	⋯
378-036277	N	3.40 ± 0.14	$\geqslant 537.19$[a]	⋯	⋯	⋯	⋯	$27.33^{+0.33}_{-0.61}$	0.92	$\geqslant 0.06$	1.00
378-036328	M	7.926 ± 0.066	$43.544^{+0.018}_{-16}$[a]	$0.317^{+0.025}_{-0.16}$	$1.598^{+0.47}_{-0.075}$	$-2.02^{+0.15}_{-0.59}$	$6.981^{+0.12}_{-0.084}$	$36.08^{+0.23}_{-0.26}$	1.10	$0.129^{+0.081}_{-0.016}$	1.00
378-036814	M	6.91 ± 0.11	235^{+26}_{-23}[a]	$0.53^{+0.24}_{-0.32}$	$3.80^{+0.81}_{-0.38}$	$-0.82^{+0.40}_{-1.1}$	$3.1^{+3.3}_{-1.0}$	$36.10^{+0.48}_{-0.33}$	0.86	$0.113^{+0.12}_{-0.042}$	1.00
379-035545	N	4.26 ± 0.21	$\geqslant 208.73$[a]	⋯	⋯	⋯	⋯	$114.9^{+1.2}_{-3.0}$	0.81	$\geqslant 0.02$	2.33
379-035649	M	4.372 ± 0.094	15.3982 ± 0.0017	0.262 ± 0.011	$0.173^{+0.019}_{-0.018}$	-1.075 ± 0.022	$11.828^{+0.080}_{-0.078}$	$35.921^{+0.037}_{-0.038}$	0.97	$0.172^{+0.11}_{-0.022}$	1.00
379-035884	N	19.03 ± 0.24	$\geqslant 574.15$	⋯	⋯	⋯	⋯	$59.1^{+1.4}_{-2.6}$	1.30	$\geqslant 0.22$	1.08
379-036194	N	4.12 ± 0.20	133^{+114}_{-66}[a]	$0.74^{+0.10}_{-0.14}$	$2.35^{+0.76}_{-1.2}$	$0.38^{+0.16}_{-0.13}$	1.85 ± 0.10	$105.73^{+0.34}_{-0.17}$	0.90	$0.0357^{+0.022}_{-0.0051}$	1.43
379-036197	N	6.603 ± 0.070	$325.9^{+9.4}_{-8.9}$[a]	$0.72^{+0.14}_{-0.31}$	$1.48^{+1.3}_{-0.89}$	$-0.43^{+0.37}_{-0.67}$	67^{+166}_{-43}	27^{+38}_{-17}	1.17	$0.67^{+0.22}_{-0.23}$	8.64

Note.
[a] Denotes target with a multimodal fit

(This table is available in its entirety in machine-readable form.)

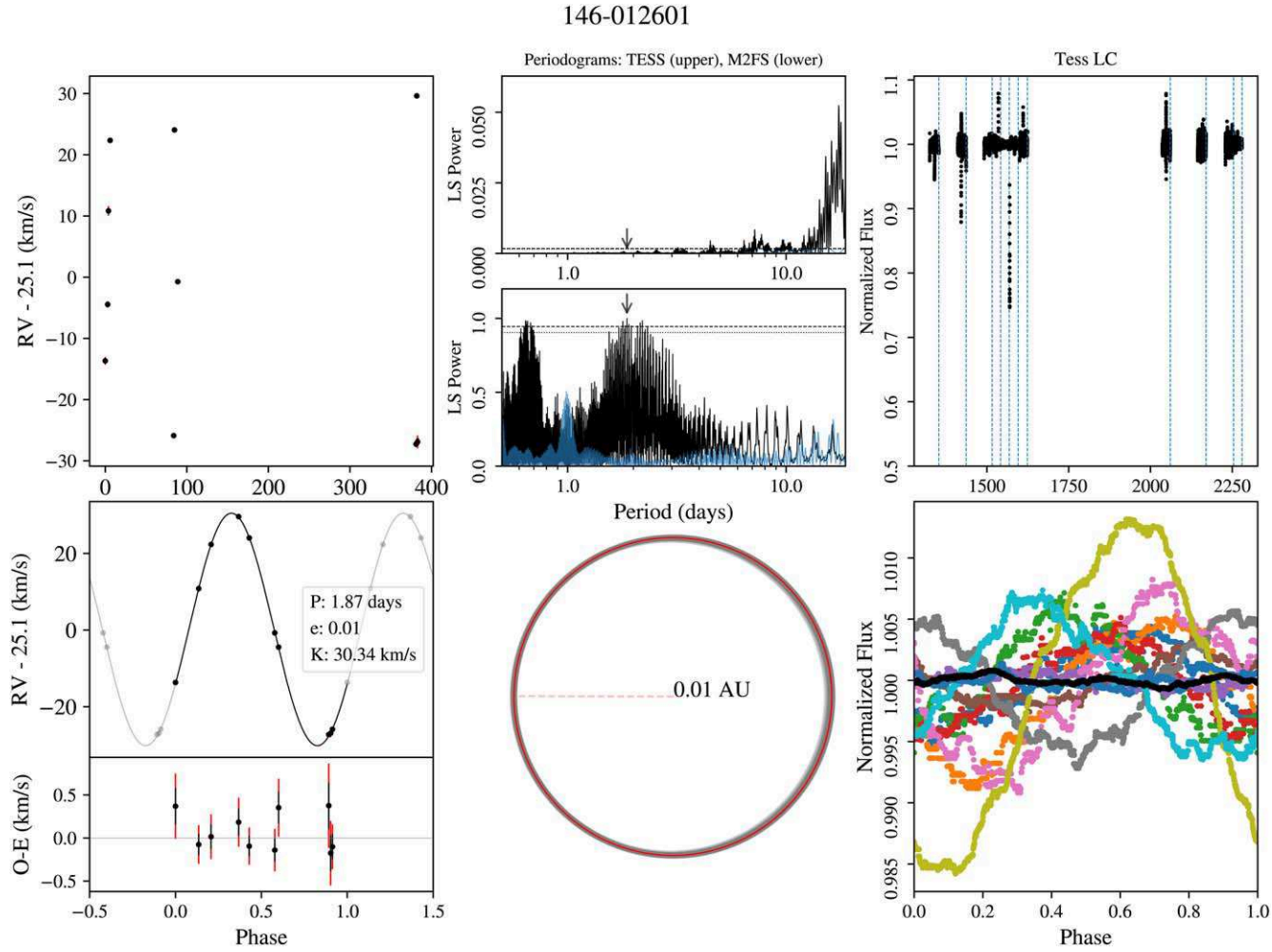

Figure 3. 146-012601, a $V = 13.9$ member of NGC 2516. The primary has a $T_{\rm eff}$ of 5116 ± 19 K, a $v_r \sin(i)$ of 16.1 ± 0.2 km s^{-1}, and a mass of 0.82 $M_\odot$. The system orbits every $1.868567^{+0.000043}_{-0.000039}$ days ($e = 0.0051^{+0.0060}_{-0.0036}$, K = $30.37^{+0.22}_{-0.23}$ km s^{-1}, $q = 0.247^{+0.14}_{-0.031}$). The systemic RV is $25.096^{+0.057}_{-0.046}$ km s^{-1}. For this star only we have median smoothed the phase-folded TESS light curves (lower right) on a 1.5 hour cadence, coloring them by sector and in aggregate (black, foreground) to highlight both the ellipsoidal variation that is washed out by a simple phase folding of all the sector data.

of prior for K. The fits that we present here adopt a uniform prior on all parameters. With this choice, K and RV_0 enter the likelihood linearly (Wright & Howard 2009) and may be analytically marginalized out. The resulting chain stores the maximum-likelihood values of K and RV_0 at the fixed values of the other parameters.

We fit the SB2 targets with a double-component fit with an additional parameter for the ratio of the RV semiamplitudes of the primary and secondary components, equivalent to their mass ratio:

$$K_{\rm ratio} = -\frac{\mathrm{RV}_2}{\mathrm{RV}_1} = \frac{K_2}{K_1} = \frac{M_1}{M_2}. \quad (1)$$

We calculated a per-star multiplicative factor, σ_χ, which would inflate the B18 RV errors σ_i sufficiently to yield a reduced χ^2 of 1, equivalent to a χ^2 of the number of degrees of freedom. The inflation factor σ_χ is simply the square root of the computed reduced χ^2, and is reported in Tables 3 and 4 in Section 3. This ad-hoc factor accounts for sources of RV uncertainty not previously addressed. For example, a poor estimate of the photon-weighted exposure midpoint could introduce uncertainty due to stellar acceleration throughout the exposure. We fold all of these effects into σ_χ, apply it to σ_i, and rerun our chains a second time in order to derive the parameters and confidence intervals we report.

2.5. Secondary Mass Distributions

We obtain a secondary mass distribution for SB2s directly from the mass ratio parameter distribution. For the remaining systems, we compute a random mass for each step in the MCMC chain by drawing $\cos(i)$ uniformly between 0 and 1. We then use the equation for radial velocity semiamplitude

$$K = \left(\frac{2\pi G}{P}\right)^{\frac{1}{3}} \frac{M_2}{(M_1 + M_2)^{\frac{2}{3}}} \frac{\sin(i)}{\sqrt{1 - e^2}} \quad (2)$$

to obtain a secondary mass, solving directly for the case of one real root. Values for M_1 were already found in B16, as described in Section 2. Figures 6–8 show secondary mass distributions for systems which returned a usable fit (see Section 3).

3. Results

Due to varying spectral quality and survey limitations, data sets for some RV variable stars lead to higher quality fits than

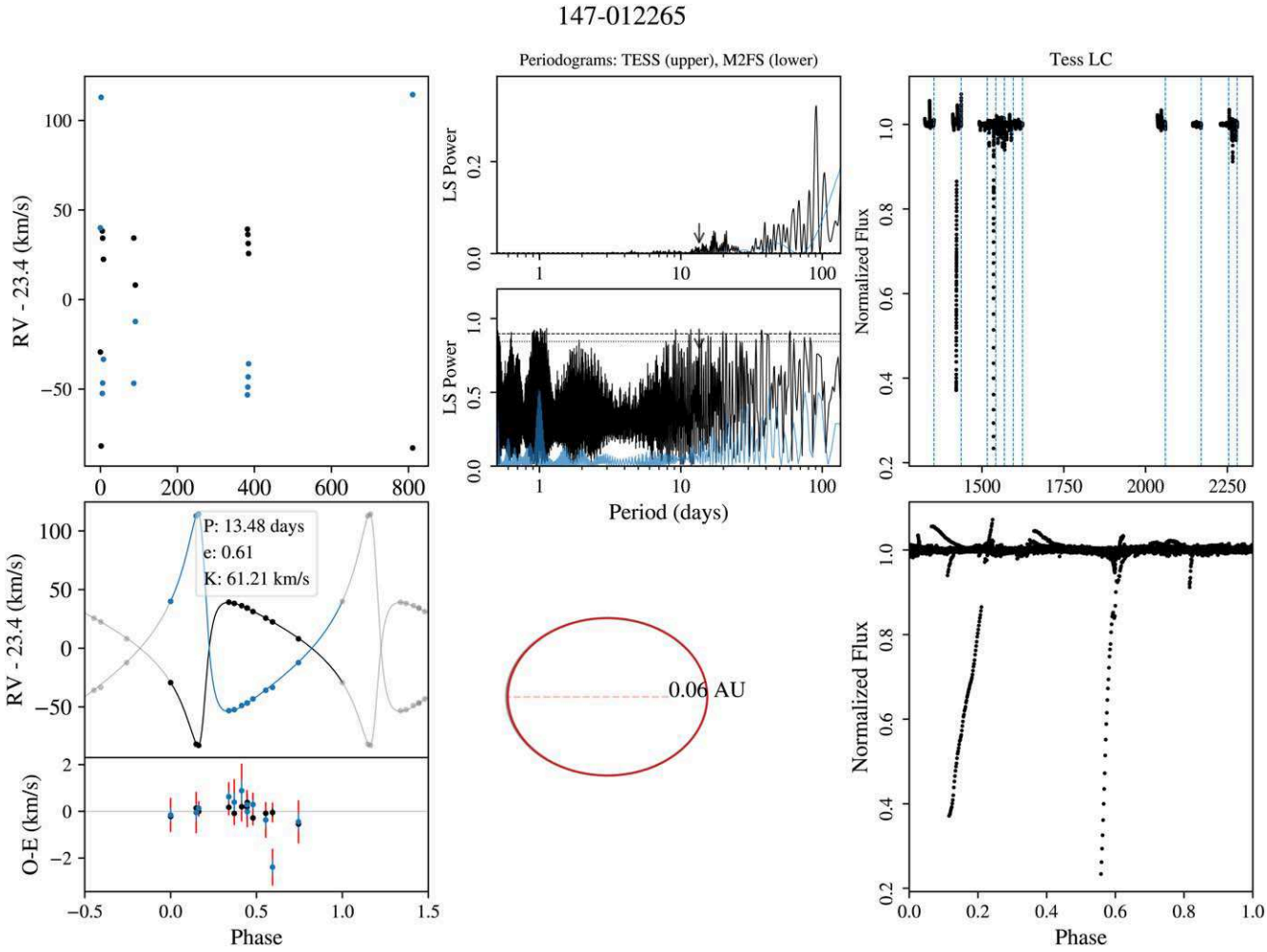

Figure 4. 147-012265, a $V = 12.1$ SB2 member of NGC 2516. The stars have a $T_{\rm eff}$ of 6482 ± 29 K and 5419 ± 88 K, a $v_r \sin(i)$ of 16.4 ± 0.1 and 13.8 ± 0.6 km s^{-1}, and masses of 1.12$M_\odot$ and 0.81 $M_\odot$. The system orbits every $13.47942^{+0.00095}_{-0.00076}$ days ($e = 0.6143^{+0.0028}_{-0.0027}$, $K_1 = 61.18^{+0.27}_{-0.22}$ km s^{-1}, $K_2 = 84.33^{+0.39}_{-0.31}$ km s^{-1}). The systemic RV is 23.424 ± 0.040 km s^{-1}.

for others. Our RV data are sparse, consisting of groups of 2–3 data points taken over a few days, with month or year-long gaps in between. For a minority of our targets this leads to aliasing and multimodal results, which we discuss on a case-by-case basis in Sections 3.2–3.4.

25 systems did not return satisfactory orbital solutions. Some returned orbits with one-day periods equivalent to the window function, or orbits which placed the companion inside the primary at closest approach. Eighteen of these systems had low-S/N ($\sigma_{\rm obs}/\sigma_{\rm meas} \leqslant 5$) RV data sets; we did not consider their data quality high enough for further exploration. Five more systems had S/Ns above this threshold, but we could not get reliable fits from the data at hand; we need either more epochs or a longer observational baseline. Some of these may simply be very active young stars. The final two systems, 147-012164 and 379-035982, stand out as systems worth further exploration because their component RVs suggest the presence of an additional companion. We discuss the status of these potentially higher-order systems in Section 3.

Tables 3 and 4 report the median values and 68% confidence intervals of the parameters for the remaining 37 systems with usable fits. These tables report target ID, member/nonmember, line-of-sight stellar rotational velocity ($v_r \sin i$), and the binary properties as obtained in 2.4. We also report the system's primary mass (M_1) and median mass ratio ($q = M_1/M_2$, see Section 2.5). SB2s are reported as "a" and "b" with shared values reported as "-". Multimodal targets have an asterisk next to their periods, quoted errors include all modes. The final column, σ_χ, gives the multiplicative constant applied to RV measurement errors to get a reduced χ^2 of ∼1. Out of these 37 systems, 11 had orbital solutions consistent with periods exceeding their observational baselines: their period posteriors lacked an upper bound. We only report the 90% lower limits of the period and mass ratio distributions for these systems, as all their other orbital parameters (with the exception of the RV_0) are poorly constrained.

3.1. Orbital Plots

Plots of the 37 systems for which we obtained a usable fit may be found in the Appendix. Three examples, Figures 3–5, are included here as they highlight target peculiarities that will be discussed in the following sections. The left column displays the RV time series (top) and the phase-folded RV with the maximum-likelihood fit and its RV residuals (bottom). The black error bars are the original RV errors from B18. The red

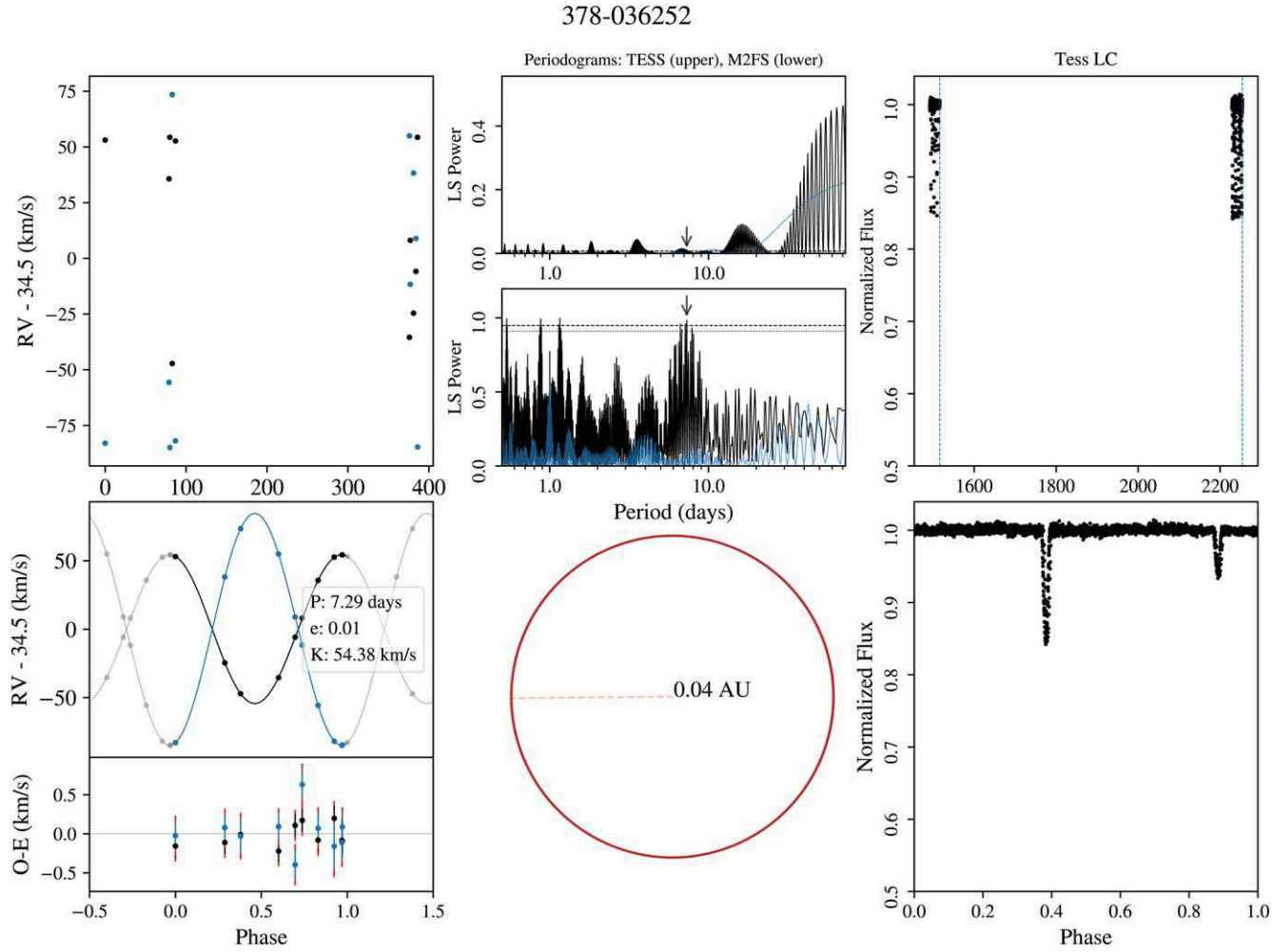

Figure 5. 378-036252, a $V = 12.5$ SB2 member of NGC 2422. The stars have a $T_{\rm eff}$ of 6495 ± 24 K and 4755 ± 78 K, a $v_r \sin(i)$ of 9.1 ± 0.1 and 6.0 ± 0.5 km s^{-1}, and masses of 1.15 $M_\odot$ and 0.74 $M_\odot$. The system orbits every 7.28663 ± 0.00010 days ($e = 0.0079 \pm 0.0014$, $K_1 = 54.39 \pm 0.11$ km s^{-1}, $K_2 = 84.73 \pm 0.16$ km s^{-1}). The systemic RV is 34.510 ± 0.018 km s^{-1}. Primary and secondary eclipses are evident in the phase-folded TESS light curve.

error margins show the extra error inflation from the per-star multiplicative factor, σ_χ.

We used `eleanor` (Feinstein et al. 2019) to download the Transiting Exoplanet Survey Satellite (TESS; Ricker et al. 2015) light curves for all available targets. We used these light curves to check for photometric periods of our binary systems and to search for eclipses or tidal ellipsoidal distortion. The right column displays these TESS light curves, with the bottom plot showing the light curve phase folded over the period.

We compute a Lomb–Scargle periodogram for each of the targets, using a maximum period of twice our observational baseline and a minimum period of half a day. We caution that periodogram peaks at or below ∼1.1 day are likely due to aliasing from our observational cadence. The center column shows Lomb–Scargle periodograms of TESS (top) and M2FS data (bottom). The dotted and dashed lines denote 95% and 99% significance, respectively, and the arrow points to the maximum-likelihood period. The faint blue lines represent their respective window functions. The bottom center plot shows a random selection of orbits from the MCMC chains with the maximum-likelihood orbit in red.

The following three subsections discuss targets of note, including those with multimodal posteriors. Corner plots for all targets with reliable orbits can be found in Appendix.

3.2. NGC 2516

1. **146-012455** (Figure A1.15), **147-012308** (Figure A1.14), **147-012175** (Figure A1.25), **147-012270** (Figure A1.30), and **148-012906** (Figure A1.13) have multimodal posterior distributions. Several have tails extending to long orbital periods. Longer orbits almost always have higher eccentricities.
2. **146-012601** (Figure A1.24) Phase-folded TESS data from sectors prior to 2021 suggested ellipsoidal variation, but this smooths out when including later data. A closer examination shows that individual sectors show strong (3%) ellipsoidal variation but with a phase and amplitude drift between sectors. For this star only we have median smoothed the phase-folded TESS light curves on a 1.5 hour cadence, coloring them by sector to highlight both the ellipsoidal variation and the phase drift.
3. **147-012164** is an SB2 for which we could not get a reliable binary fit; its stellar parameters are not stable. This is because it is a higher-order system: we see clear evidence for a third star in its spectra. The data could support a full orbital characterization with substantial extra work.

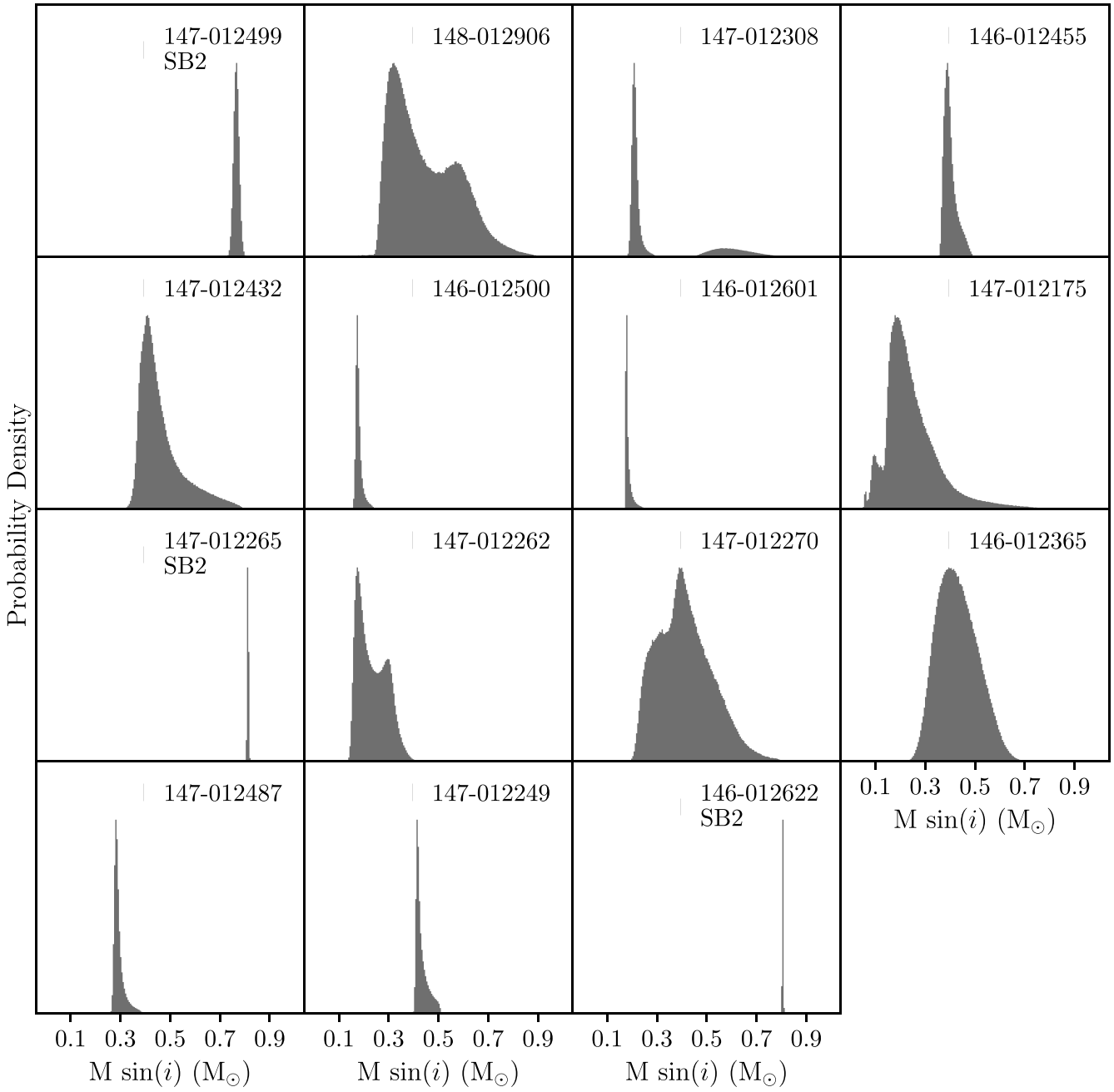

Figure 6. Secondary mass distributions for NGC 2516 members.

3.3. NGC 2422

1. **378-036328** (Figure A1.16) and **378-036814** (Figure A1.32) have multimodal posteriors; longer-period orbits have higher eccentricity.
2. **378-036252** (Figure A1.3) has a phase-folded TESS light curve, which clearly shows it to be an eclipsing binary.
3. **379-035982** is an SB2 for which we could not get a reliable binary fit. While there is no visual evidence for a third star in its spectra, this system's stellar properties and component RVs do not make sense without an additional companion. Further observations are needed in order to fully characterize this system.

3.4. Nonmembers

1. **146-012557** (Figure A1.7), **379-036194** (Figure A1.8), and **379-036197** (Figure A1.9) have multimodal posteriors; the longer-period orbits are more eccentric.

4. Discussion

Figure 10 shows the astrophysically significant parameters derived from our orbital fits: period, mass ratio, and eccentricity. Our systems span periods of two days to several years. All of the <10 day systems are nearly circular, while the wider binaries show a range of eccentricities. In this section we

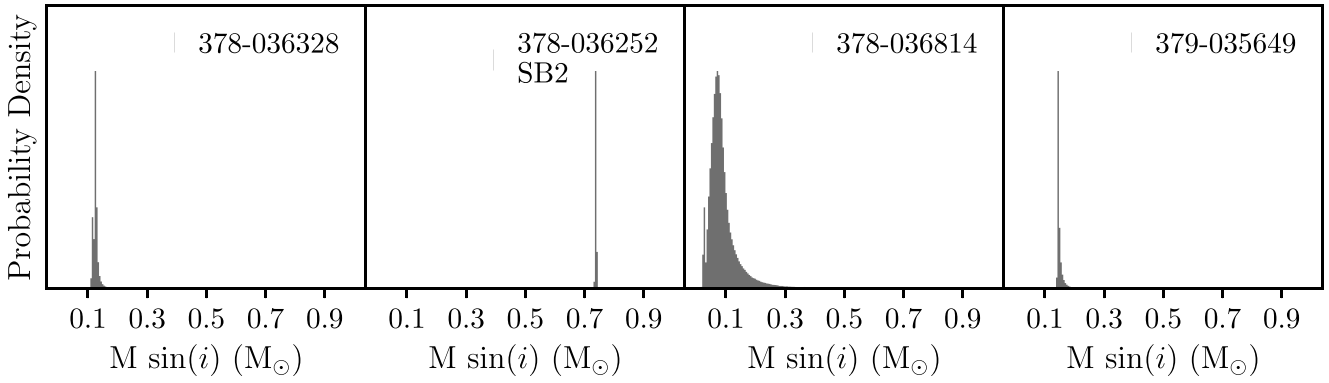

Figure 7. Secondary mass distributions for NGC 2422 members.

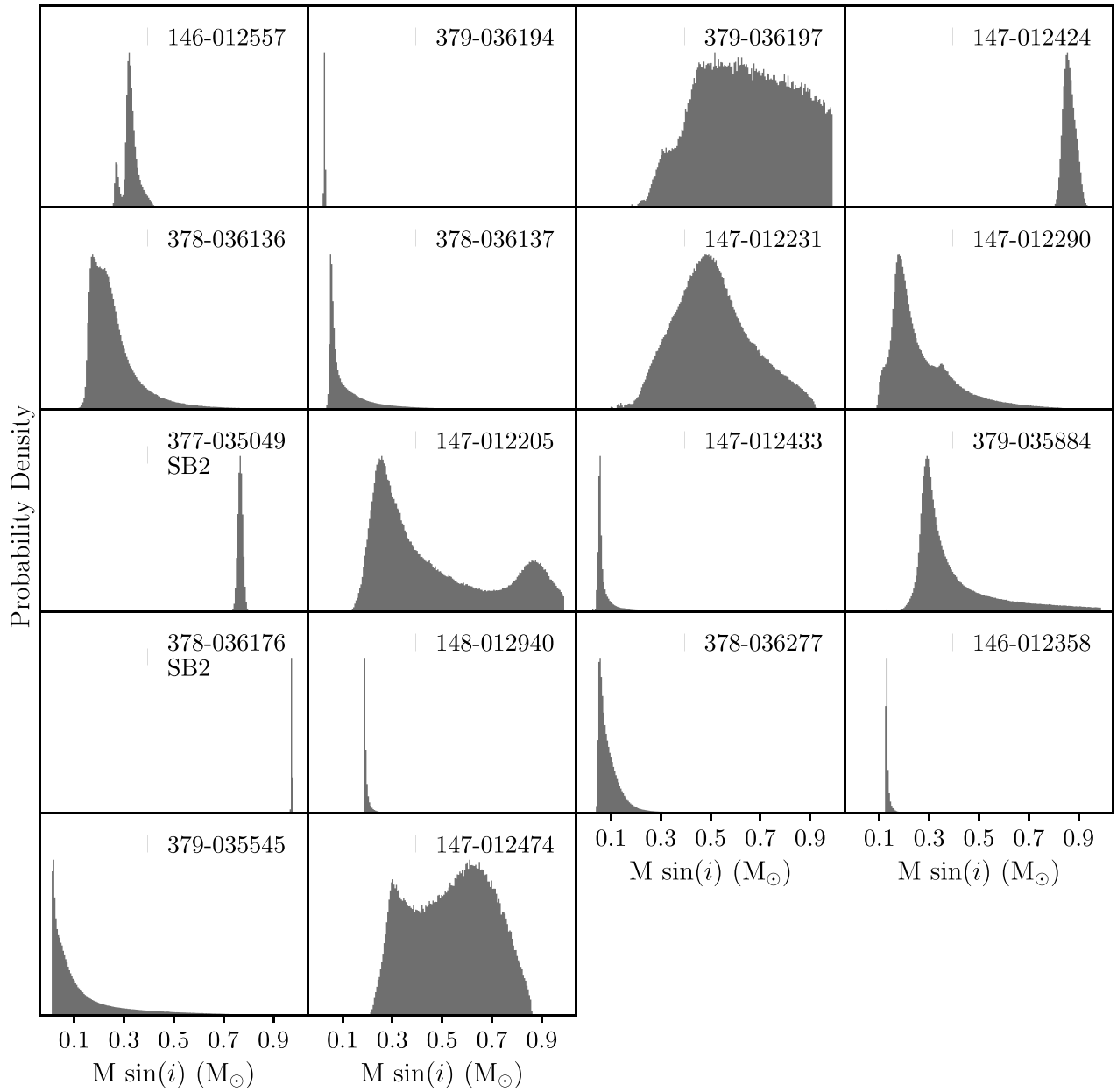

Figure 8. Secondary mass distributions for cluster nonmembers.

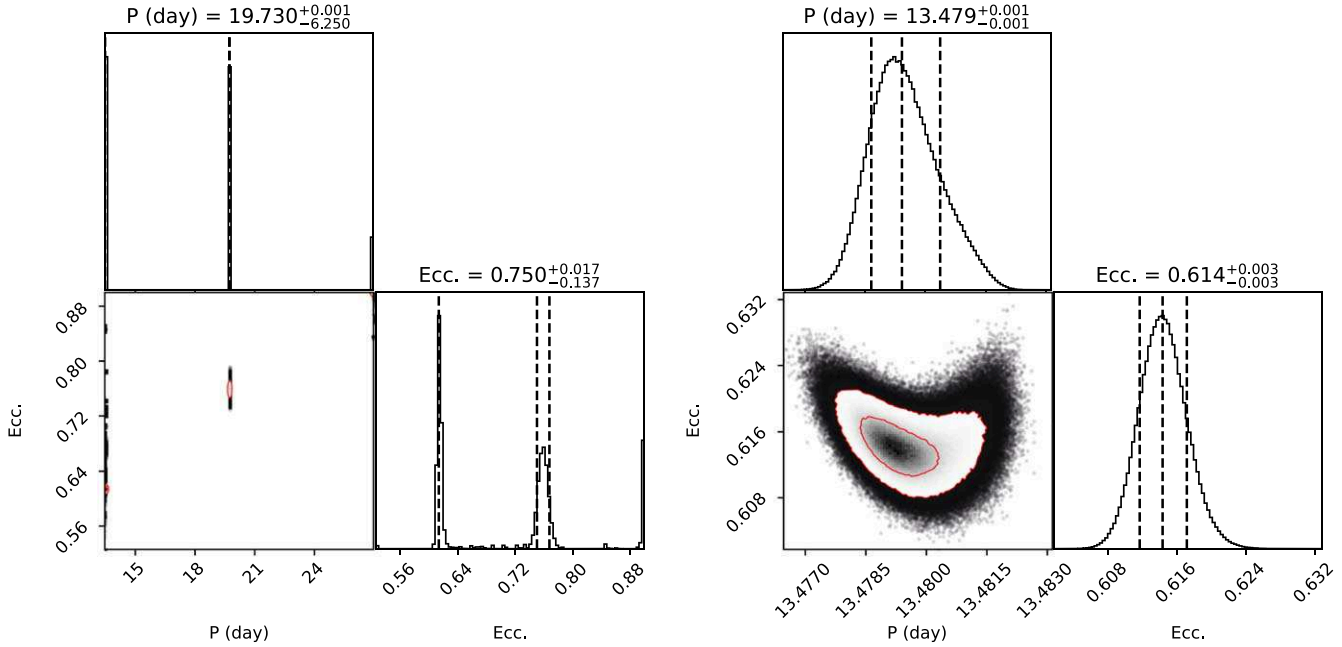

Figure 9. The period and eccentricity posteriors for NGC 2516 cluster member 147-012265 fit without (left) and with (right) a barycentric prior. The fits with the barycentric prior are well constrained and unimodal.

discuss the significance of these results for binary star formation and evolution.

4.1. Orbital Parameter Distributions: Cluster versus Field

We find that our mass ratio distributions of binaries in the clusters as well as the field (see Figure 10) are relatively flat, consistent with previous works (e.g., Raghavan et al. 2010; Duchêne & Kraus 2013). Recently, other works have noted an excess of equal-mass ($q \gtrsim 0.95$) twins at close separations (e.g., Pinsonneault & Stanek 2006; Simon & Obbie 2009; Kounkel et al. 2019) on top of a uniform distribution for systems with $q < 0.95$. While our sample size is insufficient to statistically measure a twin excess, two of our NGC 2516 SB2s, 146-012622 and 147-012499, have mass ratios of 0.97 and 0.93, respectively. Two field SB2s 377-035049 and 378-036176, are close-in binaries with mass ratios of 0.99 and 0.94, respectively.

We note an excess of short-period ($P < 100$ days) binaries along the cluster members, while most systems with periods exceeding our observational baseline are cluster nonmembers. The physical explanation for this effect is likely that these stars, which have a magnitude consistent with an FGK star at ∼450 pc despite being distant background stars, are giants that cannot physically support short-period companions.

4.2. Gaia EDR3 and RV Binary Characterization

We use the high-precision parallaxes and proper motions from Gaia EDR3 to definitively establish cluster membership. This enables us to impose a prior on the radial velocity of a system's barycenter when fitting the orbit of an astrometric member. As a result, four cluster members which originally had multimodal posteriors ended up with well-constrained and unimodal posteriors following the application of this prior. Stars reported as multimodal have errors encompassing all modes. See the corner plots in Figures A1.15 (target 146-012455) and A1.16 (target 378-036328) for two example multimodal targets. Figure 9 shows an example of this effect for NGC 2516 member 147-012265. The application of a prior effected reliable, unimodal fits for some of our notable systems, examples being 146-012601, a tight circular binary (P∼2 days), and 146-012622, an equal-mass SB2. 147-012265, an eccentric SB2, had over five visible orbital modes originally, but the application of the prior identified the dominant mode. As we discuss in the following section, 147-012265 is the shortest-period eccentric binary in our sample.

4.3. Tidal Circularization

Binary stars exert tidal forces on each other, causing them to *circularize* over time, i.e., approach a state where stellar rotation is synchronous with binary orbital motion and the stellar rotation axis is aligned with the normal to the orbital plane of motion (Mazeh 2008). Eccentricity damps due to the mismatch between the orbital frequency, which varies with orbital phase if $e > 0$, and the rotational frequency of either star.

Orbital characterization of binary star systems in open clusters enables us to determine the transition period separating circular from eccentric binaries. For example, Mathieu et al. (2004) determined the tidal circularization cutoff period for NGC 188 (∼6 Gyr) to be around 15 days using spectroscopic binaries. Meibom & Mathieu (2005)'s sample of transition periods for 8 coeval systems shows a tendency for longer transition periods in older clusters. Geller et al. (2021) recently found a tidal circularization cutoff period of $11^{+1.1}_{-1.0}$ days for open cluster M67 (∼4 Gyr), in agreement with the value of $12.1^{+1.0}_{-1.5}$ days found by Meibom & Mathieu (2005). All the clusters in the sample in the age range of NGC 2516 and NGC 2422 have cutoff periods within the 5-15 day window.

We find two binaries within this period window: 147-012265, a SB2 in NGC 2516 ($e \sim 0.61$, $P \sim 13.48$ days), and 378-036252, a circular binary in NGC 2422 ($P \sim 7.29$ days). Both of these systems are consistent with previous work. Meibom & Mathieu (2005) find a tidal circularization cutoff period for M35,

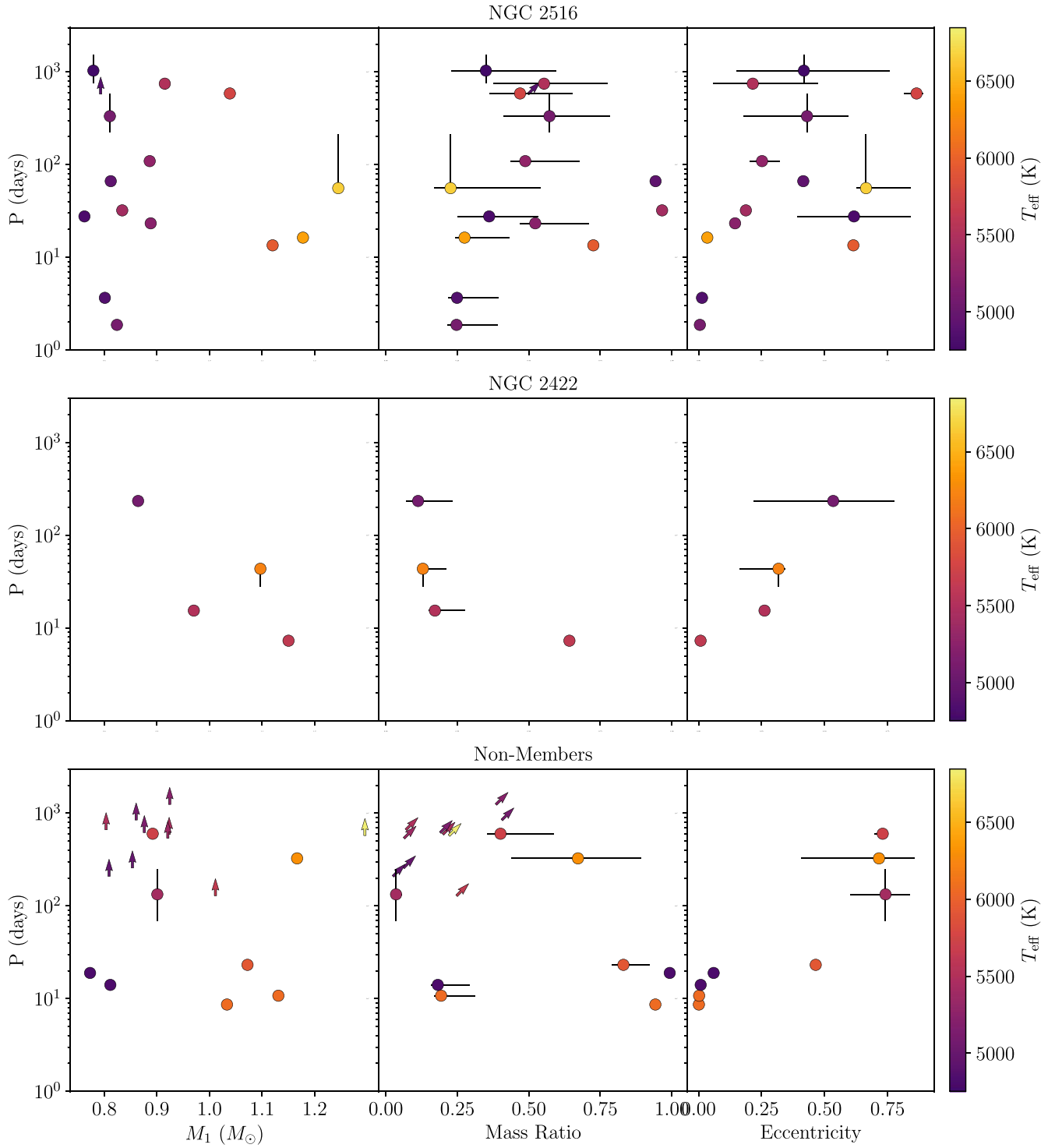

Figure 10. Scatter plots of the physically meaningful binary parameters for members of NGC 2516 and NGC 2422 (top and middle rows) and nonmembers (bottom row). The markers are colored according to the temperature of the primary star. The panels from left to right display in turn the system's primary mass, median mass ratio (M_2/M_1), and median eccentricity plotted against the median period, with $\pm$ 1σ errors. We represent the 11systems with weakly constrained orbital solutions with an arrow placed at the 90% quantile lower limit in the mass-period and mass ratio-period plots only.

a cluster around the same age as NGC 2516 and NGC 2422, of 10.2 days. Notably, all stars in their M35 sample with periods under 20 days are less eccentric than 147-012265. The discovery of other systems in NGC 2516 and NGC 2422 within this period window, particularly short-period eccentric binaries, would help constrain the transition period for these clusters. 147-012265 and 378-036252, however, could contribute to a meta-analysis looking at binaries within this crucial period window along with other systems from clusters of similar ages.

4.4. Substellar Companions

The dearth of stars with a companion mass in the brown dwarf range (5–80 $M_{\rm Jup}$) is known as the "brown dwarf desert" (Marcy & Butler 2000). Less than 1% of Sun-like stars have

brown dwarf companions according to Grether & Lineweaver (2006).

Consistent with the brown dwarf desert, almost all of our well-constrained binaries have stellar companions. Only one field star, 379-036194, has a secondary with a median derived mass of 0.036 solar masses, which is below the hydrogen-burning limit. Recent work by Fontanive et al. (2019) found that a significant fraction of brown dwarf desert inhabitants are themselves members of higher-order systems. This provides additional motivation for the full characterization of the higher-order systems we introduced in Section 3, 147-012164 and 379-035982, to determine if either of these might have a substellar companion.

5. Conclusion

In this paper we derive the Keplerian orbital parameters of 37 binary stars in the young open clusters NGC 2516 and NGC 2422. The systems span periods of two days to several years, mass ratios from ∼0.1 to unity, and eccentricities up to ∼0.9. One of these systems, 147-012265, has an unusually high eccentricity of 0.62 given its 13.48 day orbital period. Another, 378-036252, is an eclipsing binary; TESS will enable a more complete characterization. One nonmember system, 379-036194, has a companion with a secondary mass in the brown dwarf range. We are not able to reliably fit two systems, 147-012164 and 379-035982, as binaries. Their RVs indicate they are higher-order systems and require either substantial more work or spectroscopic observations for complete characterization.

We use precise stellar parallaxes and proper motions from Gaia EDR3 to definitively determine target membership status. Thanks to the Gaia EDR3 astrometric membership, we impose an extra barycentric prior on all cluster members in the fitting process. This transformed the multimodal posteriors seen in several systems before the application of the prior into well-constrained and unimodal solutions. We urge future cluster surveys to incorporate Gaia EDR3 astrometry to set an informative prior on the barycenter RV of cluster members.

We find that the mass ratio distribution for binaries across the clusters and the field is relatively flat, consistent with previous works. We identify four nearly equal-mass binaries (two in NGC 2516 and two in the field). We also find an overabundance of long-period systems in the field relative to the clusters. This is likely a selection effect: many of these field stars are background giants that are physically unable to have short-period companions.

Finally, we find two systems with periods between 5 and 15 days, which is the critical window from Meibom & Mathieu (2005) in which the tidal circularization cutoff period separating circular from eccentric binaries was found for clusters of a similar age to our own. One of them, 378-036252, is a circular binary in NGC 2422 with a period around 7 days. The other, the ∼13.5 day NGC 2516 SB2 147-012265, is more eccentric than all similar-period systems found by Meibom & Mathieu (2005) in M35 (a cluster of a similar age to NGC 2516). These binaries should be included in future analyses of circularization across similarly-aged clusters.

I.L. acknowledges support by the U.S. National Science Foundation (NSF) Graduate Research Fellowship under grant No. 1650114. Any opinions, findings, and conclusions or recommendations expressed in this material are those of the author and do not necessarily reflect the views of the NSF.

M.M. acknowledges financial support from grants AST-1312997, AST-1726457 and AST-1815403 awarded by the NSF.

I.U.R. acknowledges financial support from grants PHY-1430152 (Physics Frontier Center/JINA-CEE), AST-1613536, and AST-1815403 awarded by the NSF. This work has made use of data from the European Space Agency (ESA) mission Gaia (https://www.cosmos.esa.int/gaia), processed by the Gaia Data Processing and Analysis Consortium (DPAC; https://www.cosmos.esa.int/web/gaia/dpac/consortium). Funding for the DPAC has been provided by national institutions, in particular the institutions participating in the Gaia Multilateral Agreement.

This work has also used `eleanor`, a light-curve extraction tool for TESS Full-Frame Images, as presented in Feinstein et al. (2019).

This research made use of Astropy,[4] a community-developed core Python package for Astronomy (Astropy Collaboration et al. 2013, 2018).

Appendix

We present the orbital plots for the 37 systems for which we obtained a usable fit in the figure set for Figure A1. The left column displays the RV time series (top) and the phase-folded RV with the maximum-likelihood fit (bottom). The very bottom plot displays the RV residuals from the fit. The black error bars are the original RV errors from B18. The red error margins show the extra error inflation from the per-star multiplicative factor, σ_χ.

The center column displays TESS Lomb–Scargle periodogram (top) and M2FS LS periodograms (bottom). The dotted and dashed lines denote 95% and 99% significance, respectively. Each peridogram has an arrow hovering over the maximum-likelihood period. The faint blue lines represent the window functions of the TESS and M2FS observations. The bottom plot in the center column shows a selection of orbits explored in the MCMC fitting process, with the maximum-likelihood orbit in red. The right column displays the TESS light curves made using `eleanor`, with the bottom plot showing the light-curve phase-folded over the period.

The text descriptions under the plots summarize the results of the fit, quoting each parameter's median value from the MCMC fit with errors representing $\pm 1\sigma$ values, assuming normalcy. The text descriptions also include updated membership status and some important notes about each target originally reported in B18, such as primary star temperature and rotational velocity.

[4] http://www.astropy.org

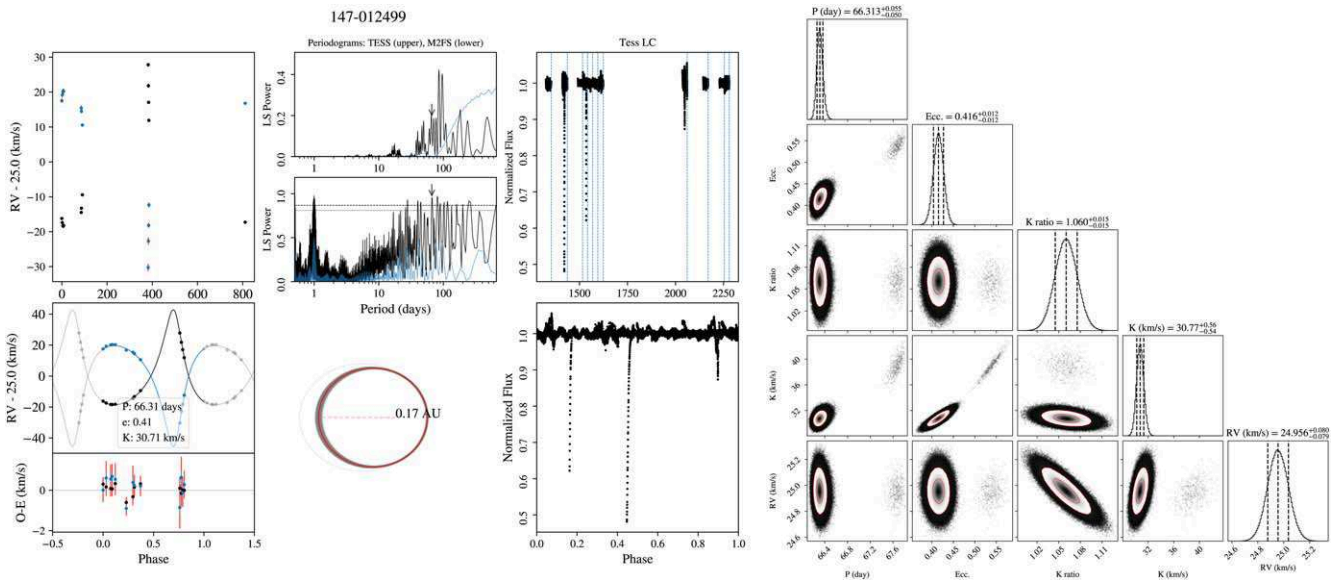

Figure A1. Sample figure from Figure Set 1. 147-012499, a $V = 13.5$ SB2 member of NGC 2516. The stars have a $T_{\rm eff}$ of 5119 ± 16 K and 4780 ± 29 K, a $v_r \sin(i)$ of 4.9 ± 0.2 and 10.1 ± 0.2 km s^{-1}, and masses of $0.81 M_{\odot}$ and $0.77 M_{\odot}$. The system orbits every $66.313^{+0.055}_{-0.050}$ days ($e = 0.416 \pm 0.012$, $K_1 = 30.77^{+0.56}_{-0.54}$ km s^{-1}, $K_2 = 32.62^{+0.61}_{-0.60}$ km s^{-1}). The systemic RV is $24.956^{+0.080}_{-0.079}$ km s^{-1}. The TESS light curves show a periodic modulation of the primary star's flux. The complete figure set (37 images) is available in the online journal.

(The data used to create this figure are available.)

(The complete figure set (37 images) is available.)

ORCID iDs

Isabel Lipartito https://orcid.org/0000-0003-4792-6479
John I. Bailey III https://orcid.org/0000-0002-4272-263X
Timothy D. Brandt https://orcid.org/0000-0003-2630-8073
Benjamin A. Mazin https://orcid.org/0000-0003-0526-1114
Mario Mateo https://orcid.org/0000-0002-3856-232X
Meghin E. Spencer https://orcid.org/0000-0003-1240-1939
Ian U. Roederer https://orcid.org/0000-0001-5107-8930

References

Astropy Collaboration, Price-Whelan, A. M., SipHocz, B. M., et al. 2018, AJ, 156, 123
Astropy Collaboration, Robitaille, T. P., Tollerud, E. J., et al. 2013, A&A, 558, A33
Badenes, C., Mazzola, C., Thompson, T. A., et al. 2018, ApJ, 854, 147
Bailey, J. I., Mateo, M., White, R. J., et al. 2016, AJ, 152, 9
Bailey, J. I., Mateo, M., White, R. J., Shectman, S. A., & Crane, J. D. 2018, MNRAS, 475, 1609
Binney, J., & Tremaine, S. 2008, Galactic Dynamics: Second Edition (Princeton, NJ: Princeton Univ. Press)
Brandt, T. D., Dupuy, T. J., Li, Y., et al. 2021, AJ, 162, 186
Cantat-Gaudin, T., Jordi, C., Vallenari, A., et al. 2018, A&A, 618, A93
Deacon, N. R., & Kraus, A. L. 2020, MNRAS, 496, 5176
Donor, J., Frinchaboy, P. M., Cunha, K., et al. 2020, AJ, 159, 199
Duchêne, G., & Kraus, A. 2013, ARA&A, 51, 269
Feinstein, A. D., Montet, B. T., Foreman-Mackey, D., et al. 2019, PASP, 131, 094502
Fontanive, C., Rice, K., Bonavita, M., et al. 2019, MNRAS, 485, 4967
Foreman-Mackey, D., Hogg, D. W., Lang, D., & Goodman, J. 2013, PASP, 125, 306
Fritzewski, D. J., Barnes, S. A., James, D. J., & Strassmeier, K. G. 2020, A&A, 641, A51
Gaia Collaboration, Babusiaux, C., van Leeuwen, F., et al. 2018, A&A, 616, A10
Gaia Collaboration, Brown, A. G. A., Vallenari, A., et al. 2021, A&A, 649, A1
Gaia Collaboration, Prusti, T., de Bruijne, J. H. J., et al. 2016, A&A, 595, A1
Geller, A. 2013, in Setting a New Standard in the Analysis of Binary Stars, EAS Publications Series, Vol. 64, ed. K. Pavlovski et al. (Cambridge: Cambridge Univ. Press), 317
Geller, A., Hurley, J., & Mathieu, R. 2013, AJ, 145, 8
Geller, A. M., de Grijs, R., Li, C., & Hurley, J. R. 2015, ApJ, 805, 11
Geller, A. M., Mathieu, R. D., Latham, D. W., et al. 2021, AJ, 161, 190
González, J. F., & Lapasset, E. 2000, AJ, 119, 2296
Goodwin, S. 2010, RSPTA, 368, 851
Grether, D., & Lineweaver, C. H. 2006, ApJ, 640, 1051
Griffin, R. F. 2012, JApA, 33, 29
Griffiths, D. W., Goodwin, S. P., & Caballero-Nieves, S. M. 2018, MNRAS, 476, 2493
Guerrero, C. A., Orlov, V. G., Monroy-Rodríguez, M. A., & Borges Fernandes, M. 2015, AJ, 150, 16
Jeffries, R. D., Thurston, M. R., & Hambly, N. C. 2001, A&A, 375, 863
Kharchenko, N. V., Piskunov, A. E., Röser, S., Schilbach, E., & Scholz, R. D. 2005, A&A, 438, 1163
Kharchenko, N. V., Piskunov, A. E., Röser, S., et al. 2009, A&A, 504, 681
Kharchenko, N. V., Piskunov, A. E., Schilbach, E., Röser, S., & Scholz, R. D. 2013, A&A, 558, A53
Kounkel, M., Covey, K., Moe, M., et al. 2019, AJ, 157, 196
Kounkel, M., Hartmann, L., Tobin, J. J., et al. 2016, ApJ, 821, 8
Lindegren, L., Klioner, S. A., Hernández, J., et al. 2021, A&A, 649, A2
Loktin, A. V., Gerasimenko, T. P., & Malysheva, L. K. 2001, A&AT, 20, 607
Lucatello, S., Sollima, A., Gratton, R., et al. 2015, A&A, 584, A52
Marcy, G. W., & Butler, R. P. 2000, PASP, 112, 137
Martinez, C. F., Holanda, N., Pereira, C. B., & Drake, N. A. 2020, MNRAS, 494, 1470
Mateo, M., Bailey, J. I., III, Crane, J., et al. 2012, Proc. SPIE, 8446, 84464Y
Mathieu, R. D., Meibom, S., & Dolan, C. J. 2004, ApJL, 602, L121
Mazeh, T. 2008, EAS Publ. Ser., 29, 1
Meibom, S., & Mathieu, R. D. 2005, ApJ, 620, 970
Meynet, G., Mermilliod, J. C., & Maeder, A. 1993, A&AS, 98, 477
Nine, A. C., Milliman, K. E., Mathieu, R. D., et al. 2020, AJ, 160, 169
Pinsonneault, M. H., & Stanek, K. Z. 2006, ApJL, 639, L67
Poovelil, V. J., Zasowski, G., Hasselquist, S., et al. 2020, ApJ, 903, 55
Portegies Zwart, S. F., McMillan, S. L. W., & Gieles, M. 2010, ARA&A, 48, 431
Prisinzano, L., Micela, G., Sciortino, S., & Favata, F. 2003, A&A, 404, 927
Raghavan, D., McAlister, H. A., Henry, T. J., et al. 2010, ApJS, 190, 1

Ricker, G. R., Winn, J. N., Vanderspek, R., et al. 2015, JATIS, 1, 014003
Sales Silva, J. V., Peña Suárez, V. J., Katime Santrich, O. J., et al. 2014, AJ, 148, 83
Simon, M., & Obbie, R. C. 2009, AJ, 137, 3442
Sollima, A., Carballo-Bello, J. A., Beccari, G., et al. 2010, MNRAS, 401, 577
Sung, H., Bessell, M. S., Lee, B.-W., & Lee, S.-G. 2002, AJ, 123, 290
Torres, G., Andersen, J., & Giménez, A. 2010, A&ARv, 18, 67
Vesperini, E., McMillan, S. L. W., D'Antona, F., & D'Ercole, A. 2011, MNRAS, 416, 355
Vesperini, E., McMillan, S. L. W., D'Antona, F., & D'Ercole, A. 2013, MNRAS, 429, 1913
Vousden, W. D., Farr, W. M., & Mandel, I. 2016, MNRAS, 455, 1919
Wright, J. T., & Howard, A. W. 2009, ApJS, 182, 205